Computers in Biology and Medicine 168 (2024) 107755

Contents lists available at ScienceDirect

Computers in Biology and Medicine

journal homepage: www.elsevier.com/locate/compbiomed

Standardized 2D atrial mapping and its clinical applications

Tiantian Wang [a], Joël Karel [a,*], Eric Invers-Rubio [c], Ismael Hernández-Romero [b], Ralf Peeters [a], Pietro Bonizzi [a], Maria S Guillem [b]

[a] Department of Advanced Computing Sciences, Maastricht University, The Netherlands
[b] ITACA Institute, Universitat Politècnica de València, Valencia, Spain
[c] Arrhythmia Unit, Hospital Clínic de Barcelona Cardiovascular Institute (ICCV), Universitat de Barcelona, Barcelona, Catalonia, Spain

ARTICLE INFO

Keywords:
2D atrial mapping
Atrial fibrillation
ECG-imaging

ABSTRACT

The visualization and comparison of electrophysiological information in the atrium among different patients could be facilitated by a standardized 2D atrial mapping. However, due to the complexity of the atrial anatomy, unfolding the 3D geometry into a 2D atrial mapping is challenging. In this study, we aim to develop a standardized approach to achieve a 2D atrial mapping that connects the left and right atria, while maintaining fixed positions and sizes of atrial segments across individuals. Atrial segmentation is a prerequisite for the process. Segmentation includes 19 different segments with 12 segments from the left atrium, 5 segments from the right atrium, and two segments for the atrial septum. To ensure consistent and physiologically meaningful segment connections, an automated procedure is applied to open up the atrial surfaces and project the 3D information into 2D. The corresponding 2D atrial mapping can then be utilized to visualize different electrophysiological information of a patient, such as activation time patterns or phase maps. This can in turn provide useful information for guiding catheter ablation. The proposed standardized 2D maps can also be used to compare more easily structural information like fibrosis distribution with rotor presence and location. We show several examples of visualization of different electrophysiological properties for both healthy subjects and patients affected by atrial fibrillation. These examples show that the proposed maps provide an easy way to visualize and interpret intra-subject information and perform inter-subject comparison, which may provide a reference framework for the analysis of the atrial fibrillation substrate before treatment, and during a catheter ablation procedure.

1. Introduction

Atrial Fibrillation (AF) is the most common cardiac arrhythmia and is characterized by a rapid and uncoordinated rhythm with no apparent discernible pattern [1]. AF is a risk factor for stroke [2], and the electro-structural remodeling undergone by the atrial substrate during AF can lead to other cardiac malfunctions and pathologies [3]. Common ways to treat AF include pharmacological cardioversion, electrical cardioversion, and catheter ablation. In the latter, a catheter is used to create scars around the Pulmonary Veins (PVs) and at other locations of the atrial myocardium identified as possible sources of AF, to block the propagation of the abnormal electrical activities [4]. This is generally guided by a 3D electroanatomical mapping system, through which the 3D atrium and the catheter position can be shown on screen. Among all, this procedure requires frequent interactions between the electrophysiologist and the clinical technician, so that the technician can move and rotate the 3D view of the atrium, and display the current region of interest [5]. Another limitation is that the 3D mapping is subject specific, making inter-subjects comparison challenging. This may limit the possibility and add the complexity when attempting to generalize an effective ablation strategy over different patients having individual 3D geometries.

In this respect, an unfolded and standardized 2D atrial mapping could assist the ablation procedure without the need for extra interaction, and allow for atrial anatomies from different patients to be displayed in a consistent way across patients. The concept of standardized 2D maps is already common for ventricular anatomies. A standardized circular uniform plot was adopted by the American Heart Association (AHA) [6] to display the left ventricle, consisting of 17 segments. Currently, it has been widely used as a simplified and standard visualization tool for reporting functional information. More recently, an open-source algorithm called UNISYS was developed [7] to display both left and right ventricles in the same circular bullseye plot. Electrical, mechanical, or anatomical data can be visualized in this plot.

* Corresponding author.
E-mail address: joel.karel@maastrichtuniversity.nl (J. Karel).

https://doi.org/10.1016/j.compbiomed.2023.107755
Received 8 June 2023; Received in revised form 10 October 2023; Accepted 20 November 2023
Available online 24 November 2023

Similarly, a uniform 2D plot of the atria could be equally relevant. However, the atrial geometry is more complex, with large variations among individuals [8]. Several methods have been proposed to generate standardized 2D maps of the atria. In [9], the wrapped contours were generated along the trimmed left atrial surface and then unfolded into the irregular 2D atrium at uniform intervals. In [5], a fixed rectangular layout of the left atrium was used to display scars, electrical information, and catheter position. This method tries to find a trade-off between area-preservation and angle-preservation, while balancing the distortion. However, the 2D atrial mapping generated by the above two methods are not uniform among different patients. For example, the position of the PVs may vary among different individuals. In [10], a uniform 2D disk of the left atrium was proposed, with the left atrium divided into 24 segments and with each PV transformed into a spaced circle and the Left Atrial Appendage (LAA) to an ellipse. This standardized representation is highly suitable for detailed inter-patient comparison tasks. Moreover, the representation into different segments helps describe the regional distribution of the functional information. While the above study focused on the left atrium, it is important to point out that also the right atrium remodeling may be a key factor in AF maintenance [11]. In [12], two different disks were developed with predefined contours of cavity for both atria, respectively. However, in this study the two atria are fully disconnected. In [13], a 2D coordinate system was developed for both the left and the right atrium. This patient specific bilayer biatrial geometry can be used as a 2D atrial visualization tool including information both about repolarization heterogeneity and fiber direction. However, the position and size of different segments may vary among different subjects, and in this method as well the two atria are fully disconnected. Still, the connection between left and right atrium is also relevant, as it has been shown that ablating Inter-Atrial Connections (IAC) contributes to the normal heartbeat recovery of the right atrium [14]. Overall, despite providing an unfolded 2D atrial mapping, none of the above methods can produce a standardized 2D atrial mapping, with the left and the right atrium connected, and with all atrial segments in fixed positions, and with fixed sizes.

In this study, we propose a method to generate a standardized 2D atrial mapping of the left and right atrium connected to one another, which maintains positions and relative sizes of different atrial segments fixed among different individuals, also preserving individual-specific structural information. The algorithm takes the 3D atrial segmentation as input, along with the vertices and their connections (faces). The proposed algorithm is fully automated. This standardized atrial mapping could be used to help guide catheter ablation and facilitate application of a specific successful ablation procedure across different patients. This is relevant since even though PVI is one of the common strategies to treat AF [15], around 60% of patients show AF recurrence [16] in the time after catheter ablation. Atrial substrates beyond the PVs [17] may contribute to AF, making the treatment of AF complex and tricky. A standardized atrial map could be used to register electrophysiological and structural information in the same plot in the 2D screen to investigate the mechanisms of AF. In addition, in recent works Deep Neural Networks (DNNs) have been used to predict endocardial voltages [18], and Convolutional Neural Network (CNNs) [19] have been proposed as an auxiliary tool to design personalized AF ablation therapy. In this respect, a standardized 2D atrial mapping could facilitate the training of deep neural networks while preserving the relevant information about a specific cardiac pathology and the corresponding patient population. Furthermore, digital twins of the atrium, encompassing structural information, electrical activities, and functional characteristics, have been extensively explored and integrated with machine learning and deep learning techniques [20]. By enabling early detection of abnormalities, personalized identification of AF mechanisms and therapeutic strategies [21], the integration of digital twin-oriented research into the intelligence platform offers a valuable tool for improving the healthcare system in the era of Artificial Intelligence (AI) [22]. Within this context, a 2D atrial mapping, coupled with anatomical and functional data, may serve as a simplified digital twin of the 3D atrium. Due to its reduced memory utilization and parameter requirements in comparison to the 3D atrium, it can facilitate real-time data processing and accelerates network training [23] on the integrated intelligence platform [24].

The paper is structured as follows: In Section 2 we introduce the method of turning the 3D atrium into a Standardized 2D Atrial Mapping (S2AM). In Section 3, we describe the clinical data, and the experiments and analyses we performed to interpret the 2D atrial map. The results are presented in Section 4 with clinical applications. After the discussion in Section 5, we conclude that the proposed method provides a standard visualization tool to investigate the atrial information from 2D atrial maps in Section 6.

All code related to the approach proposed in this study is available in Gitlab: standardized-2d-atrial-mapping.git

2. Standardized 2D Atrial Mapping

The Standardized 2D Atrial Mapping (S2AM) we propose takes a 3D atrial geometry and unfolds it into a standardized 2D atrial representation. We assume that the 3D atrial geometry has already been divided into distinct atrial segments which consist of mesh points and triangular faces. Then the process of unfolding the 3D atrium automatically is implemented from the perspective of each segment, such that all segments are transformed into 2D rectangles. The S2AM algorithm is written in MATLAB R2019a and the pipeline is illustrated in Fig. 1.

In our application, the atria are divided into 19 different segments (Fig. 1(a)). There are 12 segments from the left atrium (named segment 1-6, 8-12, LAA [25]), five from the right atrium (LVC, LW, VES, CTI and RAA [26]), and two segments for the atrial septum. Segmentation was generated automatically by using the ADAS 3D software (Galgo Medical, Barcelona, Spain). For detailed description of these segments, please refer to Appendix A.

As illustrated in Fig. 1, the S2AM process consists of five steps: faces reassignment, opening of the segments LAA and RAA, splitting of segment 12 from the LA into two graphs, unfolding of the 3D segments into 2D square segments by means of Tutte Embedding, and merging of all 2D standardized segments into a unified 2D atrial mapping. The main concepts of these five steps are described below.

2.1. Faces reassignment

The segmented 3D atrial geometries from different subjects may differ in how adjacent segments are connected to each other. For example, while segments 5 and 12 are always connected to each other, the connection between segments 3 and 12 may be different among subjects (no connection, a connecting polyline, or a single intersection vertex, as shown in Fig. 1(b)). In order to generate a standardized 2D atrial representation, all mismatches in segment connections need to be solved and uniformized.

In this step, eight pre-defined groups (see Appendix A.3) are considered. Within each group, a pairwise examination of nonadjacent segments is performed, identifying any intersection vertices shared by both segments. If more than one intersection vertex exists, the faces connected to these intersection vertices within one of the two segments are then reassigned to one segment other than the initial two segments. For instance, for group 1 in Fig. 1(b), composed by segments 3, 5, 12 and LPV, there are several intersection vertices between segment LPV and segment 5, but no intersection vertices between segment 3 and segment 12. The faces connected to these intersection vertices in segment LPV are reassigned to segment 12. Through this process, it is ensured that segments within the same group share a common vertex after faces reassignment.

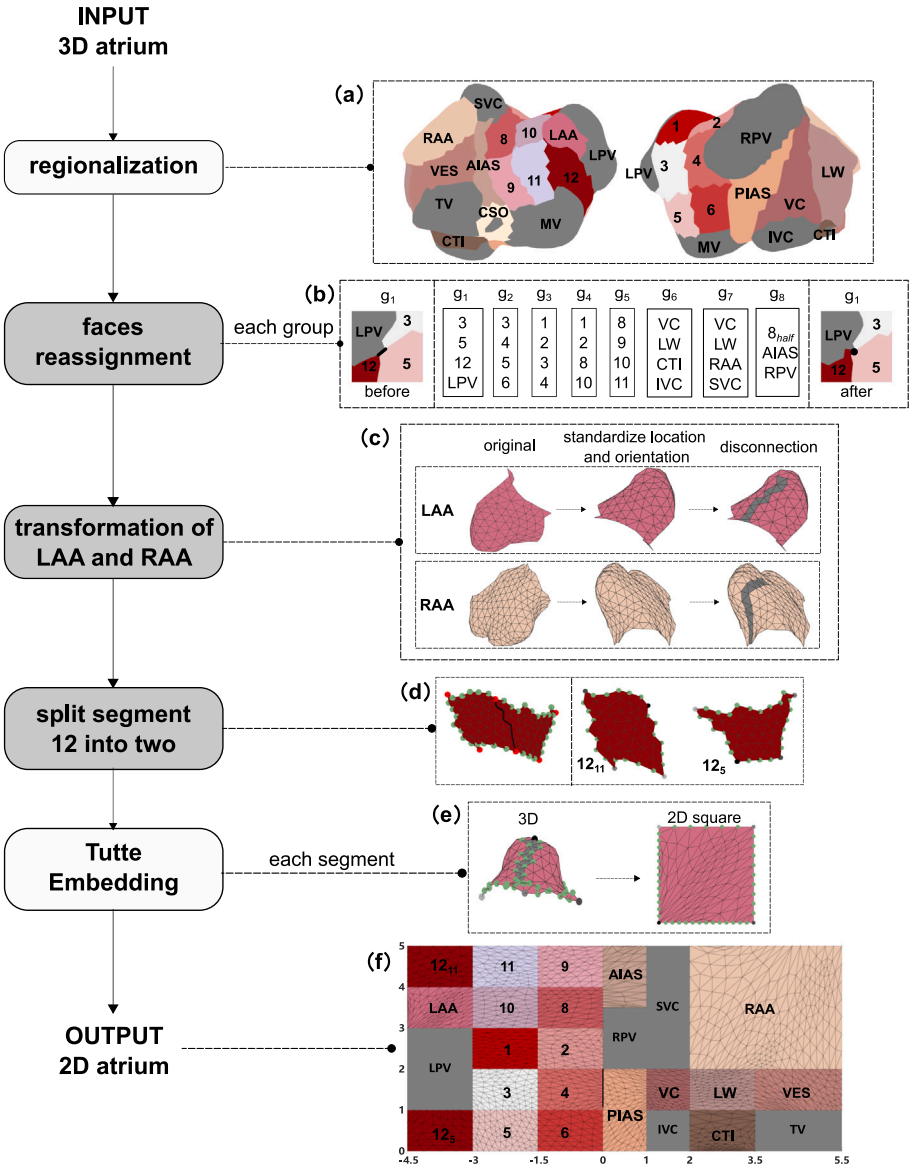

Fig. 1. Flow diagram of Standardized 2D Atrial Mapping (S2AM). The atrium includes 19 segments with 12 segments from the LA [25], 5 segments from the RA [26] and 2 segments from the inter-atrial septum. The S2AM consists of five steps. Step 1: reassign the faces for each group of segments g_i, $i = 1, \ldots, 8$ to make sure the adjacent segments in each group share one and only one intersection vertex. Step 2: after achieving the standard location and orientation for both segment LAA and RAA, extra boundary vertices are generated by disconnecting some faces. Step 3: split segment 12 into two graphs along the split path. Step 4: transform the 3D segment into 2D square graphs with the four corner vertices and boundary vertices determined beforehand. Step 5: merge all 19 standardized 2D segments into the final 2D atrial mapping.

2.2. Transformation of RAA and LAA

Segments RAA and LAA need to be opened from an **opening line** in order to generate more boundary vertices, through which the faces across this line are disconnected. The current boundary vertices are not enough to unfold the 3D segment into a well organized 2D rectangle. For instance, in segment RAA most of the boundary vertices are connected with segments LW and VES. After assigning these boundary vertices to the bottom side of the rectangle, there are only a few boundary vertices on the remaining three sides. As a result, the information on these three sides will be too much stretched.

To determine the **opening line** automatically, a standardized location and orientation should first be achieved by implementing the *translation and rotation* based on *three reference vertices*.

Fig. 2 shows the whole transformation process for segment LAA. This segment is shaped as a cap whose bottom can be used as a reference while selecting the *three reference vertices*. This is analogous for segment RAA. The *three reference vertices* of segment LAA are the intersection vertices of group {LAA, 1, 10}, {LAA, 11, 12} and {LAA, LPV, 12}. Finally, the *three reference vertices* for segment RAA are the intersection vertices of group {RAA, VC, LW}, {RAA, LW, VES} and {RAA, VES, AIAS}.

Translation and rotation of a segment starts by moving the center of mass of the three reference vertices to the origin. Then by rotating along different axes, the plane determined by the three vertices is made parallel to the XZ-plane. A line starting from the cap top to the middle vertex between the first and second reference vertex is chosen as the **opening line**. The extra boundary vertices are generated by disconnecting the faces across this line.

2.3. Splitting segment 12

Segment 12 should be split into two regions following the split path. This is required since this segment is connected to segments 5, 11 and

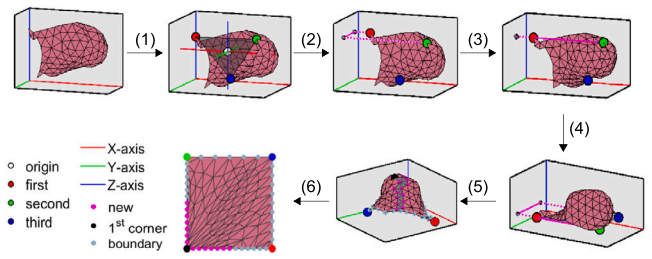

Fig. 2. The transformation process for segment LAA. White point: origin. Red vertex: first reference vertex. Green vertex: second reference vertex. Blue vertex: third reference vertex. Black vertex: the first corner. Gray vertices: boundary vertices. Magenta vertices: new-generated boundary vertices. Red line: X axis. Green line: Y axis. Blue line: Z axis. Steps: (1) move the mass center of the three reference vertices to the origin; (2) rotate along the Y-axis to let the first and second reference vertices have the same Z value; (3) rotate along the Z-axis to let the first and second reference vertices have the same Y value; (4) rotate along the X-axis to let the plane determined by the three vertices parallel to the XY plane; (5) disconnect the faces across the opening line starting from the cap top to the middle vertex of the first and second reference vertices; (6) generate the square graph using Tutte Embedding Method.

LAA. The split path is decided by the shortest path between the middle vertex of the intersection vertices between segments Mitral Valve (MV) and 12. The other is the intersection vertex of segments LAA, LPV and 12.

Fig. 1(d) shows the two split graphs of segment 12. The graph connected with segment 5 is named 12_5, and the other is named 12_{11}.

2.4. Turn 3D segments into 2D rectangle

Following the three steps above, each 3D segment can then be unfolded into a 2D rectangle, with the boundary vertices of two adjacent segments connected to each other.

We used the Tutte Embedding Method (TEM) [27] to achieve this (also known as the Barycentric method), as this method can satisfy the above requirements. With the boundary vertices remaining unchanged, each internal vertex is transformed into the barycenter of its adjacent vertices in the new graph. Consequently, all new vertices are inside or on the boundary, with the faces of the graph well-arranged.

While computing the new vertices using TEM, the Laplacian matrix L of a segment is first generated, $L = D - A$, with N being the number of vertices in the segment, $D_{N\times N}$ the degree matrix, representing the number of edges attached to each vertex [28], and $A_{N\times N}$ the adjacency matrix, indicating whether pairs of vertices are adjacent (denoted as 1) or not (denoted as 0) [29]. Afterward, the rows where the boundary vertices in the matrix L are located are changed to standard unit vectors, with the value in the location corresponding to a vertex equal to 1. The modified Laplacian matrix is denoted as P. Then the new vertices in the graph are computed by solving the following equation:

$$\tilde{H} = P^{-1}H \tag{1}$$

where H is an $N \times 2$ matrix with each row of boundary vertices equal to (x_i, y_i), each row of internal vertices equal to $(0, 0)$. $\tilde{H}$ is the new computed coordinate values of the N vertices. Eq. (1) has a unique solution. Fig. 3 shows the process of generating the new graph using TEM with a simplified graph as an example.

The location of the new vertices is related to the location of the boundary vertices and to how the vertices are connected to the adjacent vertices. For a specific 3D segment graph, how different vertices are connected to each other is already fixed. But the boundary vertices are located in 3D. Therefore, the boundary vertices should be mapped into 2D.

For each 3D segment, once the four corner vertices are determined, the boundary vertices can be assigned to the four sides. The four corner vertices for each segment are defined as the intersection vertices with the corresponding adjacent segments. The overall description of the location of the four corner vertices for all 19 segments is shown in Table 1 in Appendix B.

After determining the four corner vertices, the other boundary vertices are distributed uniformly on the four sides. Eq. (2) shows the coordinate values (x^l, y^l) of the boundary vertices on each side l of the square graph in a counterclockwise direction, $l = 1, 2, 3, 4$.

$$\begin{cases} x^1 = \left(0, \frac{1}{k_1}, \ldots, \frac{k_1 - 1}{k_1}, 1\right), y^1 = (0, \ldots, 0) \\ y^2 = \left(0, \frac{1}{k_2}, \ldots, \frac{k_2 - 1}{k_2}, 1\right), x^2 = (1, \ldots, 1) \\ x^3 = \left(1, \frac{k_3 - 1}{k_3}, \ldots, \frac{1}{k_3}, 0\right), y^3 = (1, \ldots, 1) \\ y^4 = \left(1, \frac{k_4 - 1}{k_4}, \ldots, \frac{1}{k_4}, 0\right), x^4 = (0, \ldots, 0) \end{cases} \tag{2}$$

where k_l is the number of boundary vertices on side l. Based on the new boundary vertices, the new internal vertices are computed using Eq. (1).

2.5. Merging all segments

In the final step, a standardized 2D atrial map is generated by merging together all 2D segments in fixed positions, as shown in Fig. 1(f). The connection between segment AIAS (anterior inter-atrial septum) and VES (vestibule) is removed in the 2D atrium to avoid connections between segments that are not adjacent in the 2D atrial map. The black line between segment PIAS (posterior inter-atrial septum) and segment 4 indicates that there is no connection. Apart from the above disconnections, all other segments are connected in the same way as they are connected in the 3D atrial geometry.

3. Analyses

The standardized 2D Atrial Mapping (S2AM) provides a uniform visualization tool for the atrium capable of comparing different subjects. All segments are turned into the standardized 2D shapes with a relative fixed size. As a result of unfolding the 3D atrium, the anatomical information of the 2D atrium is different from that of the original 3D atrium. Therefore, we looked at the anatomical variation due to the unfolding process. We then applied the proposed approach to healthy subjects and AF patients to investigate qualitatively the usefulness of the standardized map in visualizing electrophysiological and structural information about the underlying atrial substrate.

3.1. Clinical data

15 subjects with persistent AF before ablation procedure and 3 healthy subjects were included in the study. For AF subjects, Late Gadolinium Enhancement-Magnetic Resonance Imaging (LGE-MRI) was performed to recognize the fibrotic area.

With 64 body surface electrodes attached on the torso surface for all these 18 subjects, the torso geometry as well as the body surface potentials were obtained. Then together with atrial geometry, the atrial signals were reconstructed with Electrocardiographic Imaging (ECGI). As a noninvasive technique for reconstructing epicardial potentials, ECGI is widely used in research and clinical aspects. The standard ECGI uses zero-order Tikhonov regularization and the computed optimal regularization parameter to recover the epicardial potentials [30].

It should be mentioned that for all 18 subjects, the geometry of the atrium was not yet accessible at the time of performing ECGI. Therefore, an AI algorithm proprietary algorithm implemented in ACORYS (Corify Care SA, Madrid, Spain) was used to generate the atrial geometry to compute the ECGI results. This geometry is adjusted to the subjects' torso geometry and body measurements, but it is slightly different from the one obtained by MRI.

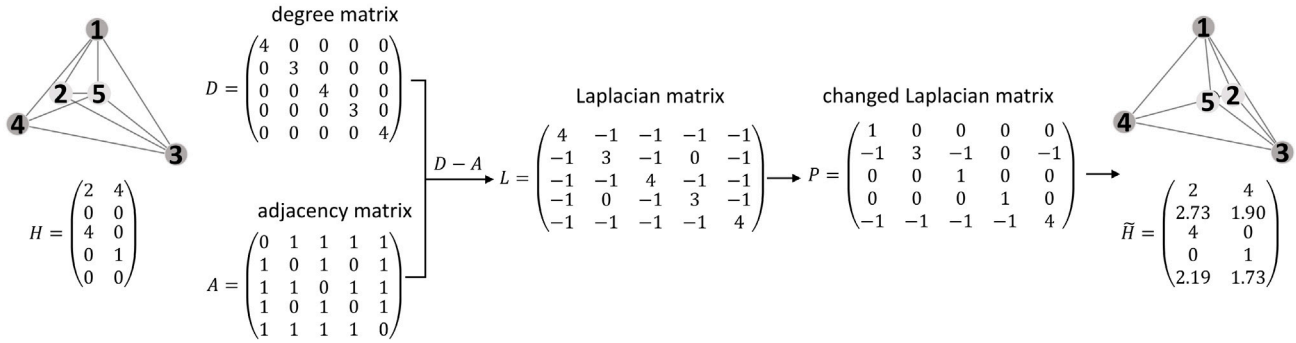

Fig. 3. Example of working of the Tutte Embedding Method. Given the graph on the left, points 1, 3, and 4 are boundary vertices, while points 2 and 5 are inner vertices. Matrix H represents the original position of each boundary vertex in the graph and zeros for the inner vertices. Based on the generated degree matrix D and adjacency matrix A, the Laplacian matrix is computed by $L = D - A$. By changing the rows where the boundary vertices are located into standard unit vectors, the matrix P is generated. Matrix $\tilde{H}$ represents the new position of each vertex in the graph.

3.2. Anatomical variation

The generation of a standardized 2D atrial mapping allows for mapping different 3D atrial segments to 2D atrial graphs such that the relative sizes and positions of those graphs are uniform across subjects. Because of the inter-individual variability in heart sizes and geometries, that means that the same 3D atrial segment from two different subjects may undergo a different amount of deformation when standardized to its corresponding 2D graph. Therefore, it is worth investigating the variability in the relative size occupied by each 3D segment in a 3D heart geometry across subjects.

For this, for each 3D atrial geometry, the size of each segment was measured as the percentage of area occupied by that segment relative to the area of all 19 segments. Regarding the area of each segment, this was computed as the sum of the surfaces of all mesh faces included in the segment.

3.3. Representing electrophysiological information onto the standardized 2D atrial mapping

The potential usefulness of the proposed standardized 2D atrial mappings to visualize electrophysiological information about the atria is shown by providing:

- Atrial mappings of Activation Times (AT) and Conduction Velocities (CV), for two healthy subjects and two AF patients, all in sinus rhythm.
- Dominant frequency distributions, and the corresponding phase maps, for an AF patient (with the phase map possibly allowing the identification of the activation patterns during AF at different time instants [31]).
- Rotor histogram and fibrosis maps, provided for two AF patients, to help investigate the relationship between the electrophysiological and the structural properties of the epicardium of a patient (the rotor histogram indicates the number of rotors in each atrial vertex [32], thus showing potential candidate locations for the generation and maintenance of the arrhythmia).

Regarding the methods for computing activation times, conduction velocities, dominant frequencies, phase maps, and rotor histograms, please refer to Appendix A.

The proposed standardized maps can also be used to visualize information about a group of subjects in a simple and efficient way. In this study, we used it to visualize whether fibrosis is present or not in a specific atrial segment, for 15 AF subjects included in the study.

4. Results

4.1. Anatomical variation

Fig. 4 shows for each subject included in this study the relative size occupied by each 3D segment in the original 3D heart geometry (as a percentage of the 19 segments). The information is shown by means of a bar graph per subject, where the colors in each bar indicate a specific atrial segment, with the same color code for the segments in Fig. 1. The size bar of the standardized 2D atrial map is also shown in the very left for comparison. In the 2D atrial map, 11 segments of the LA have an equal relative size corresponding to 3.80% of the total area. The other LA segment, segment 12 has a relative size of 7.60%. In the RA, the sizes of segment VC, LW, and VES increase in sequence, with values equal to 2.53%, 3.80% and 5.06% respectively. The RAA has the largest relative size of 26.42%. The size of segment CTI is 3.80%. Regarding the inter-atrial septum, the size of PIAS is 5.06% which is a bit larger than the size of AIAS, 3.80%. The overall sizes of the LA and the RA are 49.40% and 41.77%, respectively.

When looking at the relative sizes of the different subjects, we can notice the large variability in sizes across subjects. The sizes of the segments in the LA are generally close to each other, except for LAA, which shows a large variability across individuals. For the RA, segment LW and segment RAA are generally similar in size, and the same holds for segment VC and segment VES. At the same time, there is a large variation in the difference in size between segment LW and segment VC among different subjects.

Overall, the inter-subject variability of the atrial geometry is large, while the 2D atrium provides a standard visualization tool across subjects.

4.2. Representing electrophysiological information onto the standardized 2D atrial mapping

4.2.1. Activation time pattern

Fig. 5 shows the activation time maps and the corresponding conduction velocity maps for two healthy subjects and two AF patients, all in sinus rhythm. It can be noticed how for the first healthy subject the depolarization wavefront follows the expected physiological path (starting from an area close to the sino-atrial node, and propagating to the posterior side of the RA and to the LA).

Two depolarization breakthroughs are observed in this subject. This may be due to the early depolarization at the distal insertion of BB that intersects the LAA, which initiates the LA depolarization. The whole atrium shows a relatively homogeneous propagation with the CV close to 70 cm/s. For the area near valves, the CV is slow due to the influence of ventricular activities.

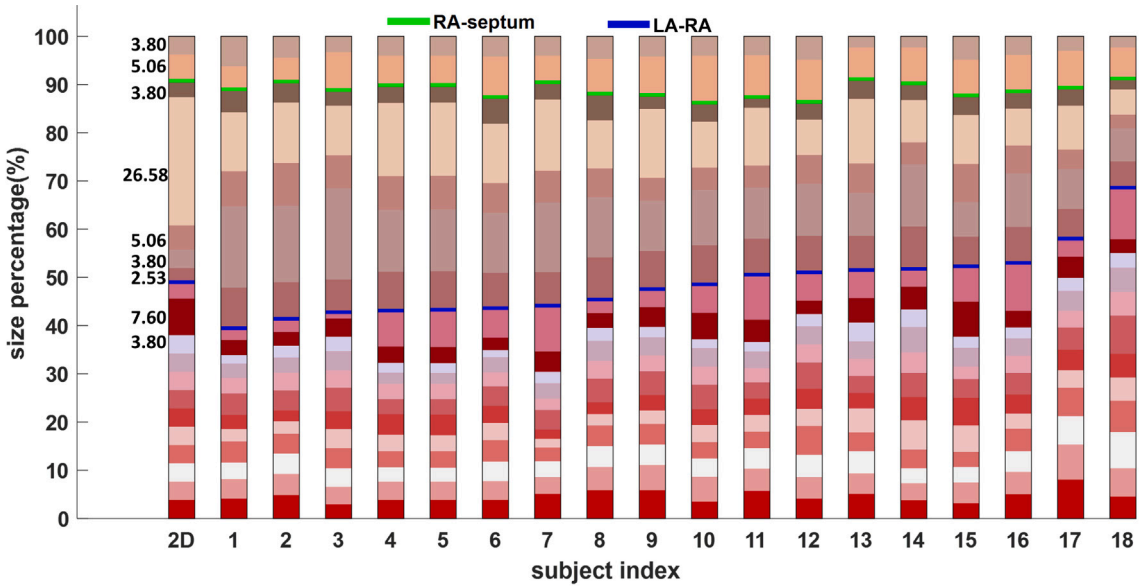

Fig. 4. The relative segment size bar for each of the 18 subjects together with the relative size bar in the 2D atrium. The blue line represents the dividing line between the LA and RA. The green line represents the dividing line between the RA and septum. The numbers to the left of the 2D atrial size bar denote the percentages of the segments. The colors match the segment colors in Fig. 1.

For the second healthy subject, the initial depolarization starts from the upper part of the PIAS which is not the anatomical location of the sino-atrial node. This mismatch may be caused by ECGI. After depolarization of the sino-atrial node, the electrical impulse propagates horizontally in the upper part of both RA and LA.

Regarding the two AF patients in sinus rhythm, the initial depolarization of both subjects starts from the upper part of PIAS due to mismatch caused by ECGI. For the first AF patient, although the propagation direction is overall similar to that of the first healthy subject, the CV is quite different. The line between the superior edges of superior PVs and the line between the inferior edges of inferior PVs show rather slow CV. The same as the floor around left inferior PV. Since the area with slow CV may indicate a candidate for catheter ablation [33], PVI could be considered as a suitable ablation procedure for this patient.

For the second AF patient, the whole atrium shows a physiological propagation. However, the floor around left inferior PV and the RAA show extremely slow CV. In general, AF patients tend to have slower CV compared with healthy subjects which is in agreement with [34].

4.2.2. Dominant frequency and phase map

Fig. 6 shows the dominant frequency map and eight snapshots of phase maps from the LA and the RA respectively, of an AF patient during an AF episode. The identified rotors are denoted by circular arrows. It can be seen that the high DF locates below the inferior edge of the inferior PV as well as on the posterior and lateral side of the RA. The migration route of rotors just surrounds the high DF area, which is in agreement with [35].

For the AF patients, the ablation creating wide area scars is more effective than the pointy ablation procedure [35]. Therefore, the mapping technique which can identify the areas contributing most to AF may be informative for such ablation procedure. The area where rotors migrate can be seen as the area that is likely to trigger AF. Therefore, since it helps understand the general rotor migration paths, the DF map may provide an additional indication for ablation procedure.

4.2.3. Fibrosis and rotors

Fig. 7 shows the extent of presence of rotors in two AF patients, both in the original 3D geometry and in the standardized 2D atrial mapping. The corresponding fibrosis distributions obtained from MRI are also shown on the right hand side of the figure. The Image Intensity Ratio (IIR) describing the pixel intensity of atrial wall normalized by blood pool intensity [36] is used to measure the amount of atrial fibrosis. A value of IIR > 1.32 may indicate dense fibrosis, $1.20 \leqslant \text{IIR} \leqslant 1.32$ indicates interstitial fibrosis, and IIR < 1.2 indicates healthy tissue. The inter-atrial septum is not available here since it was excluded from the MRI.

For the first AF patient, segment 3, segment LAA and the joint area of segment LW, VES and RAA are the three areas with a larger presence of rotors. The corresponding fibrosis mainly concentrates on segments 1, 5, 12 and RAA. For the second AF patient, the two rotor areas are segments 1 and CTI. The fibrotic areas are segments 3, 4 and 6 as well as segment VES and RAA. This shows that for these two patients, the AF rotors mostly surround the fibrotic area, which is in agreement with Cochet et al. [37]. The 3D atrial geometry with rotor mapping was generated from ECGI, while the geometry with fibrosis was generated from MRI. Therefore, the standardized 2D atrial mapping provides a tool for direct comparison between different imaging modalities.

The proposed 2D atrial mapping can also be used as an easy and efficient tool to integrate and summarize information from several subjects in the same plot. For instance, Fig. 8 shows the presence or absence of fibrosis in a specific segment for all 15 AF patients included in this study. Each dot represents a patient, and its color represents the presence (black; more than 0.5% of fibrotic tissue present) or absence (white) of fibrosis in a segment for a specific individual. The fibrotic percentage on each segment is computed as the area of fibrosis divided by the 3D atrial area with all 19 segments included. For the AF patients included in this study, it can be seen that the fibrosis is more likely to be present in the posterior wall and in the proximity of the left inferior PV in the LA. This is in line with [36]. In addition, fibrosis is preferentially located in the areas near TV in the RA.

5. Discussion

In this study, we proposed a framework for unfolding a 3D atrial geometry into a standardized 2D atrial mapping, with both atria connected. The generated map maintains a uniform structure across different subjects, despite the shape and size variations in the original 3D geometries among different individuals. Simultaneously, by preserving

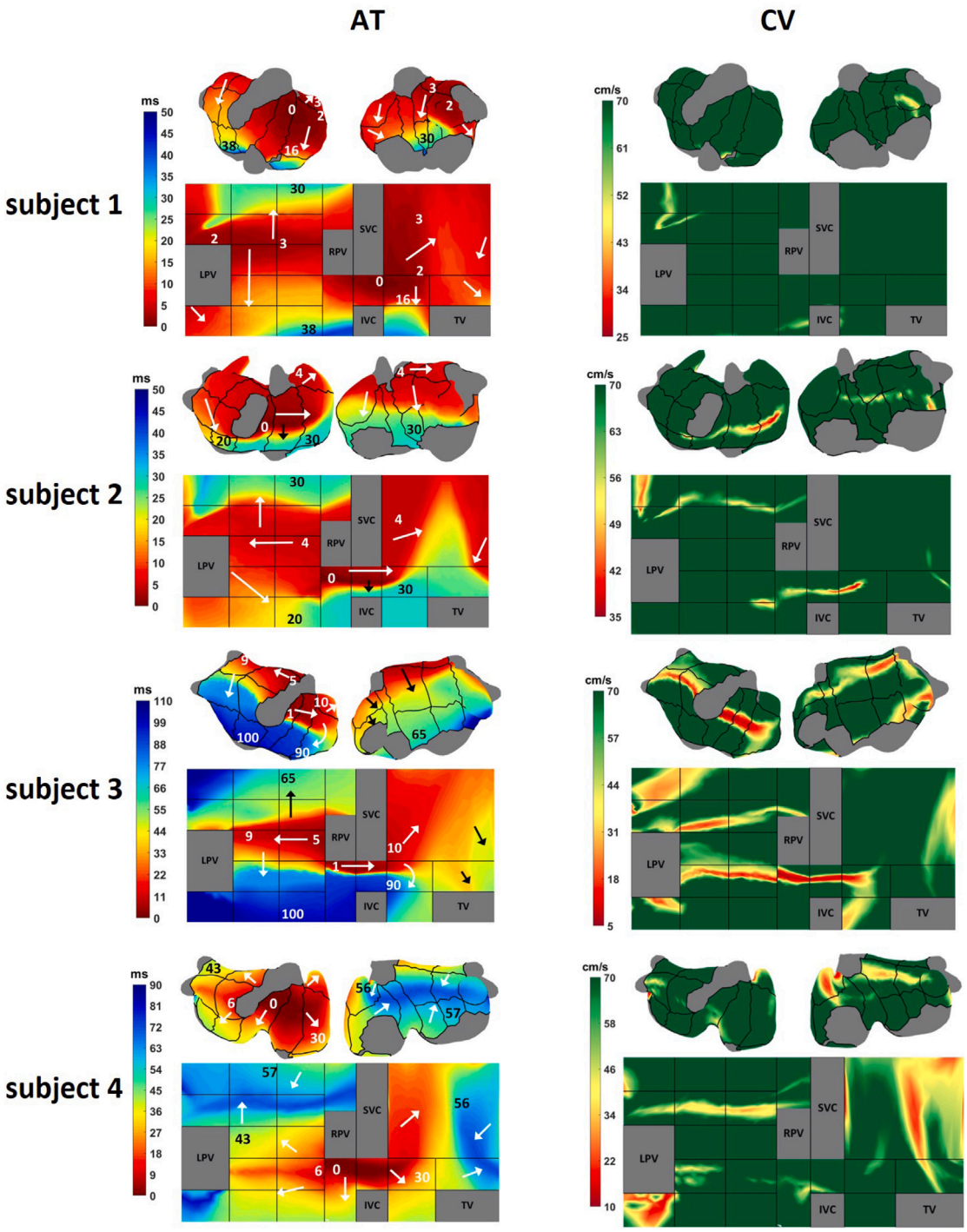

Fig. 5. 3D and 2D activation time maps (the first column) and conduction velocity maps (the second column) from two normal subjects (the first and second rows) and two persistent atrial fibrillation subjects (the third and fourth rows). The arrows represent the direction of depolarization propagation. The numbers represent the activation time(ms) for the corresponding locations. The colormap generation in MATLAB employs the default linear interpolation to produce smooth transitions between colors (the same as the figures below).

the original connections among different vertices, the 2D atrial mapping retains individual-specific structural information. The proposed algorithm requires the 3D geometry to be segmented before processing it, ensuring that the relative size of each atrial segment in the 2D map remains consistent across different subjects. By integrating and streamlining the five steps—namely, faces reassignment, opening of segments LAA and RAA, splitting of segment 12, unfolding of the 3D segments into 2D square segments, and merging, the whole process is fully automated once the 3D segmentation is available.

The proposed method differs from existing methods since it is implemented from the point of view of each segment. Some methods provide a 2D atrial mapping without any information about segmentation [5,9,13], while other methods provide segmentation of the LAA and lateral wall, but it may still be difficult to localize other atrial regions in the map [12]. The use of a segment-by-segment approach in our method is particularly beneficial when dealing with complex atrial geometries. It allows researchers to identify and isolate specific segments of interest, which can be useful in the study of AF and other

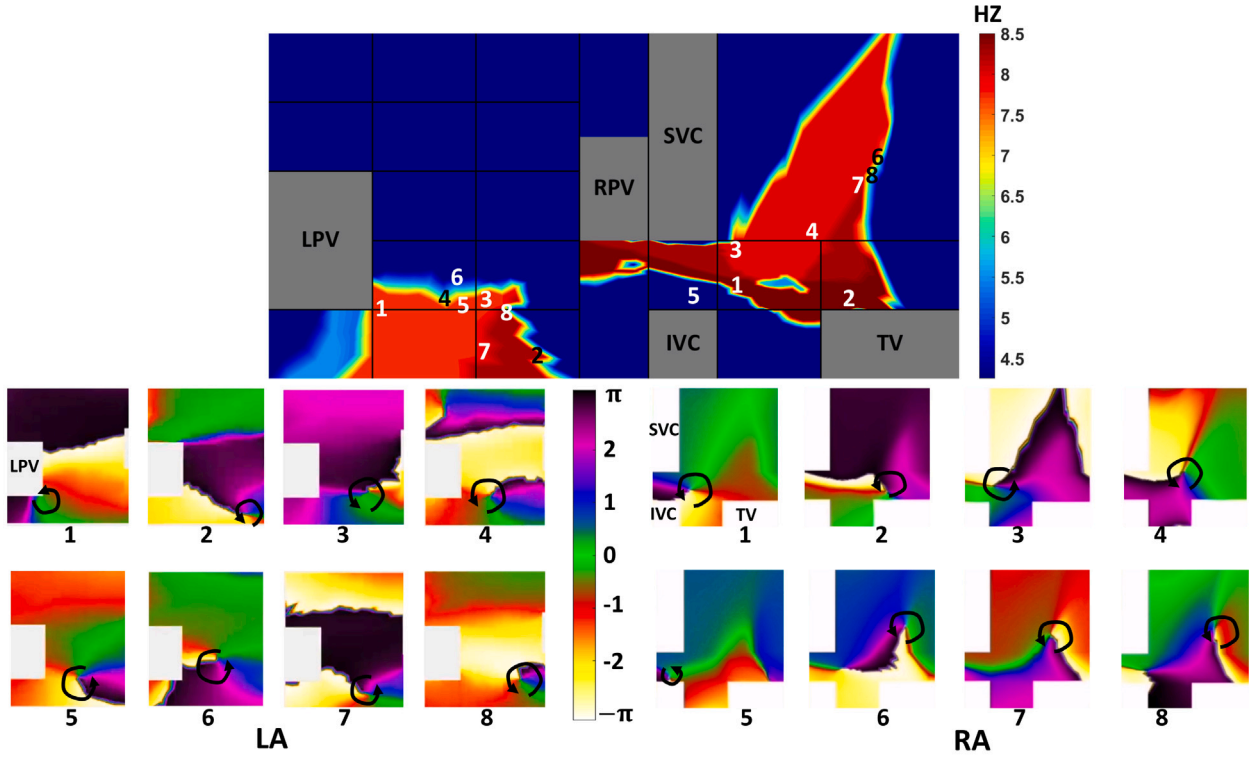

Fig. 6. Dominant frequency map and eight main snapshots of phase maps from the LA and the RA respectively. The rotated arrows in the phase maps represent the rotors. The numbers in the dominant frequency map denote the rotor locations.

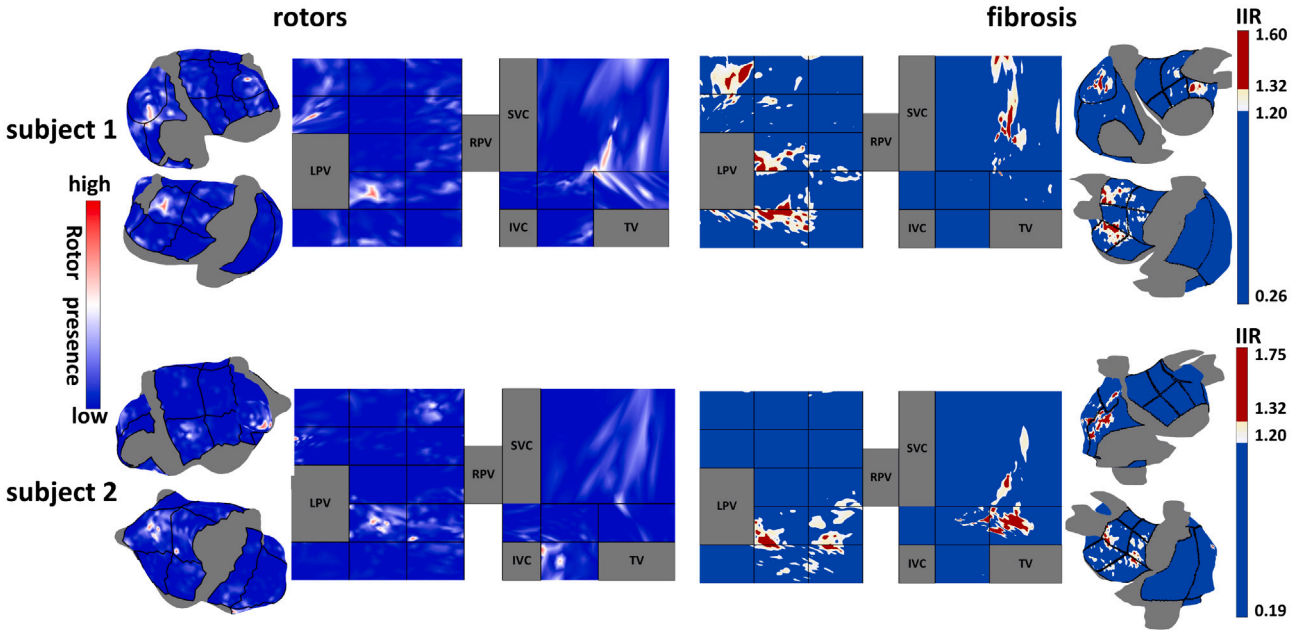

Fig. 7. 3D and 2D rotor presence maps (the first two columns) and fibrosis maps (the last two columns) from two AF subjects. For fibrosis maps, image intensity ratio (IIR) larger than 1.32 is dense fibrosis, $1.20 \leqslant \text{IIR} \leqslant 1.32$ represents interstitial fibrosis and IIR < 1.2 is healthy tissue.

cardiovascular diseases. Furthermore, the sizes and positions of both cavities and areas of interest in the 3D atrium may largely vary among different subjects. This variability, as demonstrated in [5,9], directly impacts the representation of the atrium in 2D. However, our segment-by-segment approach offers a solution by enabling us to establish consistent sizes and positions for these segments across different subjects. This streamlines the process of comparing data between different individuals.

Current methods for unfolding a 3D atrial geometry into a 2D map either focus only on the LA [5,9,10] or the LA and the RA are disconnected from one another [12,13] (no inter-atrial connections). However, RA electro-structural remodeling also contributes to AF maintenance [11] and ablation of inter-atrial connections may help to restore the normal heartbeats in the RA [14]. In our method, LA and RA are connected by the inter-atrial connections consisting of the posterior and anterior inter-atrial septum in the 2D atrial mapping. This

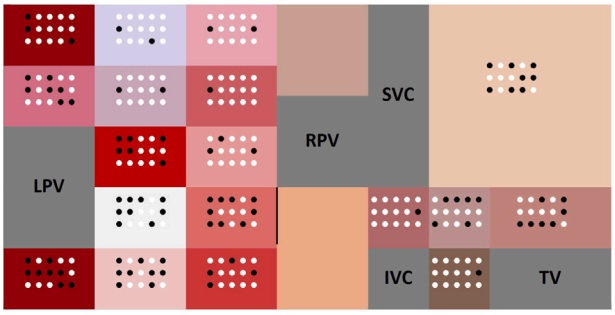

Fig. 8. Binary fibrosis labeling for all 15 AF subjects. White dots represent healthy segment. Black dots represent fibrotic segment. For the same subject, the dot in each segment shares the same location relative to the corresponding segment.

gives clinicians and researchers the possibility to observe atrial activity across both atria.

To address the issues with segmentation mismatch across different subjects, face reassignment is implemented so that adjacent segments share only one intersection vertex. This ensures that the anatomical information is totally preserved in the subsequent merging process. Furthermore, The Tutte embedding method facilitates the mapping of 3D segments into 2D segments without overlap while preserving all vertices and maintaining the original connections among different vertices. Uniform distribution of the boundary vertices ensures the alignment between adjacent segments. Due to the relatively small proportion of each face in relation to the whole area of each segment, significant distortion is avoided when applying TEM. To our knowledge, TEM has never been used in 2D atrial map.

We demonstrate the application of the standardized 2D atrial mapping by displaying different types of electrophysiological and structural information of the atrial substrate for both healthy subjects and patients affected by atrial fibrillation. In general, the proposed standardized 2D map provides a comprehensive overview of both atria, without the need to view an atrium from different angles. The different examples proposed show how the electro-structural information about the atrial activity propagation patterns and the atrial substrate is preserved when moving from a 3D geometry to the 2D map and is easily interpretable in terms of its pathophysiology properties. Moreover, we showed how the proposed standardized 2D atrial mapping is useful to easily compare information from different imaging modalities, despite the differences between the original geometries.

5.1. Limitations

The relative sizes of some segments in the proposed 2D atrial mapping do not correspond to those of the 3D atrium, as shown in Fig. 4. Some segments are stretched while other are compressed, which in turn may have an impact on the specific electrophysiological or structural information visualized on the map.

Additionally, the proposed procedure to achieve a standardized 2D atrial mapping is fully automated assuming that a segmentation of the 3D atrial geometry is already available. In line with this, the final 2D atrial mapping may depend on the specific segmentation chosen. In this study, all atrial geometries were segmented using the same strategy, and the effect of different segmentation strategies should be investigated in future studies. In addition, if this 2D atrial map is to be integrated into the catheter ablation procedure, the automatic segmentation process must also be integrated into the cardiac mapping system, ensuring its accuracy to effectively represent the 3D atrial geometry. Consequently, the integration of efficient and real-time segmentation methods into the system needs to be explored.

Furthermore, in order to attain a more precise representation of the subject-specific 3D atrial geometry, it is essential to include additional information that reflects the intricate pattern of fiber arrangement to better represent anisotropic conduction [38].

5.2. Applications

In the context of ECGI we recently showed [18] that by using deep learning it may be possible to achieve ECGI without relying on torso and heart geometry information derived from CT-scans or MRIs. To make the training of the model easier, and minimize inter-patient variability, we unfolded the 3D torso and heart geometries into 2D images, which we provided as input and output to the network, respectively. While in that study we only reconstructed electrical potentials on the ventricles, the standardized 2D atrial mapping proposed in this study could be used to extend the use of this model to the atria. By predicting the atrial electrical activities through deep learning without requiring the atrial geometry, this extension opens new possibilities for ECGI of the atrium.

Beyond its applications in ECGI, the efficient data processing and training capabilities of the 2D atrial map, coupled with its ability to generalize across diverse populations, underscore its promise in advancing our understanding of cardiac electrophysiology through deep learning. For example, this 2D atrial map can be utilized for the automated detection of AF with precise localization and the generation of patient-specific catheter ablation procedure. Its ability to capture essential features of the 3D atrium while minimizing individual variations makes the deep learning model more applicable to a broader range of patients.

Additionally, the standardized 2D atrial map assumes the role of a concise yet comprehensive digital twin of the 3D atrial geometry [20]. By accurately capturing patient-specific structural information in a 2D format, it enables real-time visualization of cardiac electrical behavior in one view, allowing for early and swift detection of abnormalities. This capability is invaluable in critical situations, facilitating immediate decision-making and intervention during medical procedures. Moreover, in the era of seamless connectivity and data exchange between medical devices and healthcare systems, the standardized 2D atrial map offers quicker data transfer and storage compared to 3D data [23]. It enables the integration of patient-specific cardiac information into the larger healthcare ecosystem with a standardized layout, enabling straightforward visualization and accurate comparison. This aspect is particularly advantageous for efficient data management in integration platforms, streamlining workflows for healthcare professionals.

From a clinical perspective, the 2D atrial map will allow integration with a wider array of medical imaging and diagnostic equipment and would potentially benefit from the fusion of different imaging technologies. Its seamless integration into existing medical workflows empowers electrophysiologists to visualize the entire atrial electrical activity in a single 2D view on-screen during the catheter ablation process, reducing the need for frequent interactions with clinical technicians. This capability is particularly beneficial for observing atrial tachycardia circuits or regions lacking propagation conduction, where seeing the mapped cycle length becomes crucial to the procedure. By visually representing conduction velocity and activation times on the standardized 2D atrial map, clinicians can quickly identify regions of abnormal conduction or delayed activation, which are often indicative of substrate for AF maintenance [34]. The 2D atrial map can also illustrate the structural alterations such as fibrosis map [39], highlighting areas with impaired tissue integrity that might facilitate the formation and propagation of abnormal electrical signals. Clinicians can utilize this visualization to accurately locate areas prone to re-entrant circuits and arrhythmia triggers, which are responsible for the perpetuation of AF. In essence, this enhanced visualization offers clinicians a holistic understanding of the underlying substrate for AF. This detailed insight may guide treatment decisions by enabling precise targeting of interventions, optimizing the chances of successful ablation procedures, and ultimately improving patient outcomes.

Finally, this 2D representation will allow to perform clinical studies of atrial arrhythmias, allowing for a capability of inter-patient comparison of clinically relevant metrics that is not possible with any method

currently available. While other approaches for a 2D representation of the atria have been developed [13], our method does impose restrictions on the 2D representation for all our predefined atrial regions and, therefore, allows for a pixel-by-pixel comparison of two 2D maps generated from different patients.

6. Conclusions and future work

This study proposed a novel framework to unfold a 3D atrial geometry into a standardized 2D atrial mapping. The proposed method is fully automated once a segmentation of the 3D atrial geometry is available. While maintaining consistent size and location for each segment across different individuals, the 2D atrial map also retains the subject-specific structural information. The resulting 2D atrial map exhibits minimal distortion, making it a robust, simplified, and standardized representation of the 3D atrium geometry. In the context of atrial fibrillation, it allows for an easy and effective way to visualize and investigate electrophysiological and anatomical information about the atrial fibrillation substrate. While enabling quick and straightforward inter-subjects comparison, this 2D atrial map also facilitates efficient intra-subject comparisons across diverse data sources. The proposed standardized 2D atrial mapping also holds great potential to be combined with deep learning techniques. It can be perceived as a simplified 2D digital twin of the atrium, capturing essential aspects without distinct reliance on the original 3D atrial geometry. The integration of deep learning with this 2D map can revolutionize data management in healthcare integration platforms and streamline clinical workflows, benefiting both patients and healthcare professionals.

In summary, the proposed standardized 2D atrial mapping offers a powerful tool for understanding and visualizing atrial anatomy and function. Its potential compatibility with deep learning techniques, coupled with its potential impact on healthcare integration and clinical practice, opens up exciting possibilities for advancing cardiac research and patient care.

Future investigations should also delve into leveraging the proposed standardized 2D atrial map to train deep learning models to improve understanding and treatment of AF.

CRediT authorship contribution statement

Tiantian Wang: Conceptualization, Methodology, Experiment design, Analysis and interpretation of results, Original draft, Manuscript revision. **Joël Karel:** Methodological considerations, Interpretation of results, Manuscript revision. **Eric Invers-Rubio:** Data collection, Manuscript revision. **Ismael Hernández-Romero:** Manuscript revision. **Ralf Peeters:** Methodological considerations, Interpretation of results, Manuscript revision. **Pietro Bonizzi:** Methodological considerations, Interpretation of results, Manuscript revision. **Maria S Guillem:** Conceptualization, Methodological considerations, Manuscript revision.

Declaration of competing interest

The authors declare the following financial interests/personal relationships which may be considered as potential competing interests: Maria S Guillem and Ismael Hernández-Romero are the shareholders and have received honoraria from Corify Care.

Acknowledgments

This work has been supported in part by a grant from the European Union's Horizon Research and Innovation Programme under the Marie Skłodowska-Curie Grant Agreement (no 860974). Tiantian Wang is funded by the China Scholarship Council (CSC), grant number 201908210340. We would like to thank Shuhe Zhang for the fruitful discussions on the methods and algorithms.

Appendix A

A.1. Description of 19 segments

Segment 1-4 = posterior wall bounded by LPV-LA line, RPV-LA line, superior edge of superior PV and inferior edge of inferior PV;
segment 5 and 6 = two equal-sized segments bounded by inferior edge of inferior PV and posterior aspect of mitral valve (MV);
segment 8-11 = anterior wall bounded by superior edge of superior PV and anterior aspect of mitral valve (MV);
segment 12 = left lateral wall bounded by anterior wall, the base of LA appendage (LAA) and left floor of segment 5;
segment LAA = left atrium appendage;
segment VC = vena cava;
segment LW = lateral wall;
segment VES = vestibule;
segment CTI = cavotricuspid isthmus;
segment RAA = right atrium appendage;
segment PIAS = posterior inter-atrial septum;
segment AIAS = anterior inter-atrial septum.

A.2. Size and position of different segments

The 3D atrium is expanded from the posterior septum to a 2D graph. In general, the posterior side of the atrium will be at the bottom of the 2D atrium and the anterior side at the top. The LA will be on the left side of the 2D atrium graph and the RA on the right. With segment 5 and 6 placed on the bottom, segment 1-4 and 8-11 are stacked on top following the anatomical arrangement in 3D atrium. These 10 segments are similar in size and they resemble rectangles. Therefore, in the 2D atrium graph, these 10 segments are set as rectangles of size equal to 1.5 cm × 1 cm. Segment 12 is split into two parts, each of size equal to 1.5 cm × 1 cm. One part is connected with segment 5, the other is connected with segment 11 and segment LAA which size is also 1.5 cm × 1 cm. Regarding the inter-atria septum, the width of both AIAS and PIAS is 1 cm. The left boundary of segment AIAS is connected with segment 9 and half connected with segment 8. Following the anatomical connection in the 3D atrium, segment PIAS is connected with segment 6 and partially connected with segment 4. The height of segment PIAS is equal to 2 cm. On the right boundary of PIAS, segment VC, LW and VES are connected in sequence. The height of these three segments is 1 cm and the width is 1 cm, 1.5 cm and 2 cm respectively. The 2D graph of segment VES is wider than both segment VC and LW. This is due to the anatomical shape of segment VES is more similar to a wide rectangle compared to VC and LW. Segment CTI is connected with the lower boundary of segment LW with the size being 1 cm × 1 cm. The lower boundary of segment RAA is fully connected with both segment LW and VES, with the height being 3 cm. As a result, the whole 2D atrium graph is a 10 cm × 5 cm rectangle with cavities including LPV, RPV, SVC, IVC and TV filled cohesively. The LA and RA are equal in the width and height with the value being 4.5 cm and 5 cm respectively.

A.3. Groups for faces reassignment

The faces reassignment is implemented separately by eight distinct groups, namely g_1 = {3, 5, 12, LPV}, g_2 = {3, 4, 5, 6}, g_3 = {1, 2, 3, 4}, g_4 = {1, 2, 8, 10}, g_5 = {8, 9, 10, 11}, g_6 = {VC, LW, CTI, IVC}, g_7 = {VC, LW, RAA, SVC} and $g_8 = \{8_{\text{half}}, \text{AIAS, RPV}\}$. As for group g_8, after face reassignment, segment 8 should be half connected to segment AIAS and half connected to segment RPV.

Table 1
The location of four corner vertices for 19 segments.

Segment	First	Second	Third	Fourth
1	{1,3,LPV}	{1,2,3,4}	{1,2,8,10}	{1,10,LAA}
2	{1,2,3,4}	{2,4,RPV}	{2,8,RPV}	{1,2,8,10}
3	{3,5,12}	{3,4,5,6}	{1,2,3,4}	{1,3,LPV}
4	{3,4,5,6}	{4,6,PIAS(RPV)}[a]	{2,4,RPV}	{1,2,3,4}
5	{5,12,VV}	{5,6,VV}	{3,4,5,6}	{3,5,12}
6	{5,6,VV}	{6,PIAS,VV}	{4,6,PIAS(RPV)}[a]	{3,4,5,6}
8	{1,2,8,10}	{2,8,RPV}	{8,9,AIAS}	{8,9,10,11}
9	{8,9,10,11}	{8,9,AIAS}	{9,AIAS,CSO(VV)}[a]	{9,11,VV}
10	{1,10,LAA}	{1,2,8,10}	{8,9,10,11}	{10,11,12}
11	{10,11,12}	{8,9,10,11}	{9,11,VV}	{11,12,VV}
12	{11,12,VV}	{5,12,VV}	{3,5,12}	{10,11,12}
VC	{VC,PIAS,AIAS(IVC/CSO)}	{VC,LW,CTI}	{VC,LW,RAA}	{VC,PIAS,SVC}
LW	{LW,VC,CTI}	{LW,CTI,VES}	{LW,RAA,VES}	{LW,RAA,VC}
VES	{VES,LW,CTI}	{VES,AIAS,VV(CSO)}	{VES,RAA,AIAS(SVC)}[a]	{VES,LW,RAA}
CTI	$\{\text{B-CTI}\}_{2/7}$[b]	$\{\text{B-CTI}\}_{5/7}$[b]	{CTI,LW,VES}	{CTI,LW,VC}
PIAS	{PIAS,VV,6}	$\{\text{B-PIAS}\}_{1/2}$[b]	{PIAS,VC,SVC}	$\{\text{PIAS,RPV}\}_{1/2}$[c]
AIAS	{AIAS,SVC,8}	{AIAS,VES,RAA(SVC)}[a]	{AIAS,CSO,VV(VES)}	{AIAS,9,CSO(VV)}[a]
LAA	$\{\text{B-LAA}\}_{1/2}$[b]	{LAA,1,10}	{10,11,12}	{LAA,RPV,12}
RAA	{RAA,VC,LW}	{RAA,VES,AIAS(SVC)}[a]	$\{\text{B-RAA}\}_{2/9}$[b]	$\{\text{B-RAA}\}_{7/9}$[b]

[a] Use () if {} fails.

[b] {B-CTI} represents the boundary vertices from the fourth corner to the third corner in a counterclockwise direction. {B-PIAS} represents the boundary vertices from the first corner to the first corner of segment VC in a counterclockwise direction. {B-LAA} represents the boundary vertices from the second corner to the fourth corner in a clockwise direction. {B-RAA} represents the boundary vertices from the second corner to the first corner in a counterclockwise direction. All subscripts indicates the index of the corner as a proportion of the number of boundary vertices.

[c] Middle vertex of the intersection vertices between segments PIAS and RPV.

A.4. How to compute different mapping techniques

AT is computed as the moment when the change in temporal derivative of signals matches with the change in spatial derivative [40] of atrium surface. Then for the corresponding CV, it is calculated by fitting a polynomial to the spatio-temporal coordinates of the atrial activities [41]. The DF is the frequency of the sinusoidal waveform with highest amplitude which can optimally approximate the signal [42]. A phase map with the values ranging from $-pi$ to pi enables the identification of the activation pattern in AF rhythms [31], with pi representing resting, $pi/2$ for depolarization, 0 for plateau, and $-pi$ for repolarization [43]. Finally, the rotor histogram indicates the number of rotors in each atrial mesh point [32].

Appendix B

Table 1 shows the locations of four corner vertices for 19 segments.

References

[1] S. Levy, G. Breithardt, R. Campbell, A. Camm, J.-C. Daubert, M. Allessie, E. Aliot, A. Capucci, F. Cosio, H. Crijns, et al., Atrial fibrillation: Current knowledge and recommendations for management, Eur. Heart J. 19 (9) (1998) 1294–1320.

[2] B. Freedman, T.S. Potpara, G.Y. Lip, Stroke prevention in atrial fibrillation, Lancet 388 (10046) (2016) 806–817.

[3] S. Benussi, G.E. De Maat, Atrial remodelling and function: Implications for atrial fibrillation surgery, Eur. J. Cardio-Thoracic Surg. 53 (suppl_1) (2018) i2–i8.

[4] M. Haissaguerre, P. Jaïs, D.C. Shah, A. Takahashi, M. Hocini, G. Quiniou, S. Garrigue, A. Le Mouroux, P. Le Métayer, J. Clémenty, Spontaneous initiation of atrial fibrillation by ectopic beats originating in the pulmonary veins, N. Engl. J. Med. 339 (10) (1998) 659–666.

[5] R. Karim, Y. Ma, M. Jang, R.J. Housden, S.E. Williams, Z. Chen, A. Ataollahi, K. Althoefer, C.A. Rinaldi, R. Razavi, et al., Surface flattening of the human left atrium and proof-of-concept clinical applications, Comput. Med. Imaging Graph. 38 (4) (2014) 251–266.

[6] M.D. Cerqueira, N.J. Weissman, V. Dilsizian, A.K. Jacobs, S. Kaul, W.K. Laskey, D.J. Pennell, J.A. Rumberger, T. Ryan, et al., Standardized myocardial segmentation and nomenclature for tomographic imaging of the heart: A statement for healthcare professionals from the Cardiac Imaging Committee of the Council on Clinical Cardiology of the American Heart Association, Circulation 105 (4) (2002) 539–542.

[7] J. Stoks, U.C. Nguyen, R. Peeters, P.G. Volders, M.J. Cluitmans, An Open-Source Algorithm for Standardized Bullseye Visualization of High-Resolution Cardiac Ventricular Data: UNISYS, IEEE, 2020.

[8] L. Prasanna, R. Praveena, A.S. D'Souza, K.M. Bhat, Variations in the pulmonary venous ostium in the left atrium and its clinical importance, J. Clin. Diagn. Res. 8 (2) (2014) 10.

[9] Y. Ma, R. Karim, R.J. Housden, G. Gijsbers, R. Bullens, C.A. Rinaldi, R. Razavi, T. Schaeffter, K.S. Rhode, Cardiac unfold: A novel technique for image-guided cardiac catheterization procedures, in: Information Processing in Computer-Assisted Interventions: Third International Conference, Springer, 2012, pp. 104–114.

[10] S.E. Williams, C. Tobon-Gomez, M.A. Zuluaga, H. Chubb, C. Butakoff, R. Karim, E. Ahmed, O. Camara, K.S. Rhode, Standardized unfold mapping: A technique to permit left atrial regional data display and analysis, J. Interventional Cardiac Electrophysiol. 50 (2017) 125–131.

[11] H. Hasebe, K. Yoshida, M. Iida, N. Hatano, T. Muramatsu, A. Nogami, K. Aonuma, Differences in the structural characteristics and distribution of epicardial adipose tissue between left and right atrial fibrillation, EP Europace 20 (3) (2018) 435–442.

[12] M. Nuñez-Garcia, G. Bernardino, R. Doste, J. Zhao, O. Camara, C. Butakoff, Standard quasi-conformal flattening of the right and left atria, in: Functional Imaging and Modeling of the Heart: 10th International Conference, FIMH 2019, Bordeaux, France, June 6–8, 2019, Proceedings 10, Springer, 2019, pp. 85–93.

[13] C.H. Roney, A. Pashaei, M. Meo, R. Dubois, P.M. Boyle, N.A. Trayanova, H. Cochet, S.A. Niederer, E.J. Vigmond, Universal atrial coordinates applied to visualisation, registration and construction of patient specific meshes, Med. Image Anal. 55 (2019) 65–75.

[14] C.H. Roney, S.E. Williams, H. Cochet, R.K. Mukherjee, L. O'Neill, I. Sim, J. Whitaker, O. Razeghi, G.J. Klein, E.J. Vigmond, et al., Patient-specific simulations predict efficacy of ablation of interatrial connections for treatment of persistent atrial fibrillation, EP Europace 20 (suppl_3) (2018) iii55–iii68.

[15] G. Hindricks, T. Potpara, N. Dagres, E. Arbelo, J.J. Bax, C. Blomström-Lundqvist, G. Boriani, M. Castella, G.-A. Dan, P.E. Dilaveris, et al., 2020 ESC Guidelines for the diagnosis and management of atrial fibrillation developed in collaboration with the European Association for Cardio-Thoracic Surgery(EACTS): The Task Force for the diagnosis and management of atrial fibrillation of the European Society of Cardiology(ESC) developed with the special contribution of the European Heart Rhythm Association(EHRA) of the ESC, Eur. Heart J. 42 (5) (2021) 373–498.

[16] K. Benali, V. Barré, A. Hermida, V. Galand, A. Milhem, S. Philibert, S. Boveda, C. Bars, F. Anselme, B. Maille, et al., Recurrences of atrial fibrillation despite durable pulmonary vein isolation: The PARTY-PVI study, Circulation: Arrhythmia Electrophysiol. 16 (3) (2023) e011354.

[17] A.M. Al-Kaisey, R. Parameswaran, J.M. Kalman, Atrial fibrillation structural substrates: Aetiology, identification and implications, Arrhythmia Electrophysiol. Rev. 9 (3) (2020) 113.

[18] T. Wang, P. Bonizzi, J. Karel, R. Peeters, ECGI with a deep neural network and 2D normalized body surface potential maps, in: 2021 Computing in Cardiology, Vol. 48, IEEE, 2021, pp. 1–4.

[19] M. Muffoletto, A. Qureshi, A. Zeidan, L. Muizniece, X. Fu, J. Zhao, A. Roy, P.A. Bates, O. Aslanidi, Toward patient-specific prediction of ablation strategies for atrial fibrillation using deep learning, Front. Physiol. 12 (2021) 674106.

[20] G. Coorey, G.A. Figtree, D.F. Fletcher, V.J. Snelson, S.T. Vernon, D. Winlaw, S.M. Grieve, A. McEwan, J.Y.H. Yang, P. Qian, et al., The health digital twin to tackle cardiovascular disease—A review of an emerging interdisciplinary field, NPJ Digit. Med. 5 (1) (2022) 126.
[21] L. Azzolin, M. Eichenlaub, C. Nagel, D. Nairn, J. Sanchez, L. Unger, O. Dössel, A. Jadidi, A. Loewe, Personalized ablation vs. conventional ablation strategies to terminate atrial fibrillation and prevent recurrence, Europace 25 (1) (2023) 211–222.
[22] O. Moztarzadeh, M. Jamshidi, S. Sargolzaei, A. Jamshidi, N. Baghalipour, M. Malekzadeh Moghani, L. Hauer, Metaverse and healthcare: Machine learning-enabled digital twins of cancer, Bioengineering 10 (4) (2023) 455.
[23] M.B. Jamshidi, F. Daneshfar, A hybrid echo state network for hypercomplex pattern recognition, classification, and big data analysis, in: 2022 12th International Conference on Computer and Knowledge Engineering, ICCKE, IEEE, 2022, pp. 007–012.
[24] O. Moztarzadeh, M. Jamshidi, S. Sargolzaei, F. Keikhaee, A. Jamshidi, S. Shadroo, L. Hauer, Metaverse and medical diagnosis: A blockchain-based digital twinning approach based on MobileNetV2 algorithm for cervical vertebral maturation, Diagnostics 13 (8) (2023) 1485.
[25] E.M. Benito, N. Cabanelas, M. Nuñez-Garcia, F. Alarcón, R.M. Figueras i Ventura, D. Soto-Iglesias, E. Guasch, S. Prat-Gonzalez, R.J. Perea, R. Borràs, et al., Preferential regional distribution of atrial fibrosis in posterior wall around left inferior pulmonary vein as identified by late gadolinium enhancement cardiac magnetic resonance in patients with atrial fibrillation, EP Europace 20 (12) (2018) 1959–1965.
[26] C. Gunturiz-Beltrán, M. Nuñez-Garcia, T.F. Althoff, R. Borràs, R.M. Figueras i Ventura, P. Garre, G. Caixal, S. Prat-González, R.J. Perea, E.M. Benito, et al., Progressive and simultaneous right and left atrial remodeling uncovered by a comprehensive magnetic resonance assessment in atrial fibrillation, J. Am. Heart Assoc. 11 (20) (2022) 26–28.
[27] W.T. Tutte, How to draw a graph, Proc. Lond. Math. Soc. 3 (1) (1963) 743–767.
[28] F. Chung, L. Lu, V. Vu, Spectra of random graphs with given expected degrees, Proc. Natl. Acad. Sci. 100 (11) (2003) 6313–6318.
[29] F.R. Chung, Spectral Graph Theory, Vol. 92, American Mathematical Soc., 1997.
[30] T. Wang, J. Karel, P. Bonizzi, R.L. Peeters, Influence of the Tikhonov regularization parameter on the accuracy of the inverse problem in electrocardiography, Sensors 23 (4) (2023) 1841.
[31] M.S. Guillem, A.M. Climent, M. Rodrigo, F. Fernández-Avilés, F. Atienza, O. Berenfeld, Presence and stability of rotors in atrial fibrillation: Evidence and therapeutic implications, Cardiovasc. Res. 109 (4) (2016) 480–492.
[32] M. Rodrigo, A.M. Climent, A. Liberos, F. Fernández-Avilés, O. Berenfeld, F. Atienza, M.S. Guillem, Highest dominant frequency and rotor positions are robust markers of driver location during noninvasive mapping of atrial fibrillation: A computational study, Heart Rhythm 14 (8) (2017) 1224–1233.
[33] S. Honarbakhsh, R. Schilling, M. Orini, R. Providencia, M. Finlay, E. Keating, P. Lambiase, A. Chow, M. Earley, S. Sporton, et al., Left atrial scarring and conduction velocity dynamics: Rate dependent conduction slowing predicts sites of localized reentrant atrial tachycardias, Int. J. Cardiol. 278 (2019) 114–119.
[34] A. Heida, W.F. van der Does, L.N. van Staveren, Y.J. Taverne, M.C. Roos-Serote, A.J. Bogers, N.M. de Groot, Conduction heterogeneity: Impact of underlying heart disease and atrial fibrillation, Clin. Electrophysiol. 6 (14) (2020) 1844–1854.
[35] K. Umapathy, K. Nair, S. Masse, S. Krishnan, J. Rogers, M.P. Nash, K. Nanthakumar, Phase mapping of cardiac fibrillation, Circulation: Arrhythmia Electrophysiol. 3 (1) (2010) 105–114.
[36] E.M. Benito, A. Carlosena-Remirez, E. Guasch, S. Prat-González, R.J. Perea, R. Figueras, R. Borràs, D. Andreu, E. Arbelo, J.M. Tolosana, et al., Left atrial fibrosis quantification by late gadolinium-enhanced magnetic resonance: A new method to standardize the thresholds for reproducibility, EP Europace 19 (8) (2017) 1272–1279.
[37] H. Cochet, R. Dubois, S. Yamashita, N. Al Jefairi, B. Berte, J.-M. Sellal, D. Hooks, A. Frontera, S. Amraoui, A. Zemoura, et al., Relationship between fibrosis detected on late gadolinium-enhanced cardiac magnetic resonance and re-entrant activity assessed with electrocardiographic imaging in human persistent atrial fibrillation, JACC: Clin. Electrophysiol. 4 (1) (2018) 17–29.
[38] I. Kotadia, J. Whitaker, C. Roney, S. Niederer, M. O'Neill, M. Bishop, M. Wright, Anisotropic cardiac conduction, Arrhythmia Electrophysiol. Rev. 9 (4) (2020) 202.
[39] V. Polyakova, S. Miyagawa, Z. Szalay, J. Risteli, S. Kostin, Atrial extracellular matrix remodelling in patients with atrial fibrillation, J. Cell. Mol. Med. 12 (1) (2008) 189–208.
[40] M.J. Cluitmans, P. Bonizzi, J.M. Karel, M. Das, B.L. Kietselaer, M.M. de Jong, F.W. Prinzen, R.L. Peeters, R.L. Westra, P.G. Volders, In vivo validation of electrocardiographic imaging, Clin. Electrophysiol. 3 (3) (2017) 232–242.
[41] A.R. Barnette, P.V. Bayly, S. Zhang, G.P. Walcott, R.E. Ideker, W.M. Smith, Estimation of 3-D conduction velocity vector fields from cardiac mapping data, IEEE Trans. Biomed. Eng. 47 (8) (2000) 1027–1035.
[42] J. Ng, J.J. Goldberger, Understanding and interpreting dominant frequency analysis of AF electrograms, J. Cardiovasc. Electrophysiol. 18 (6) (2007) 680–685.
[43] M. Rodrigo, A.M. Climent, A. Liberos, F. Fernández-Avilés, O. Berenfeld, F. Atienza, M.S. Guillem, Technical considerations on phase mapping for identification of atrial reentrant activity in direct-and inverse-computed electrograms, Circulation: Arrhythmia Electrophysiol. 10 (9) (2017) e005008.